Accepted Manuscript

Phase separated characteristics affected by cooling rate of immiscible Cu-Cr alloy by laser surface melting

Litian Zhang, Gang Yu, Xiuli He, Shaoxia Li, Weijian Ning, Xu Wang

PII: S0925-8388(18)32886-X

DOI: 10.1016/j.jallcom.2018.08.012

Reference: JALCOM 47100

To appear in: *Journal of Alloys and Compounds*

Received Date: 25 May 2018

Revised Date: 1 August 2018

Accepted Date: 2 August 2018

Please cite this article as: L. Zhang, G. Yu, X. He, S. Li, W. Ning, X. Wang, Phase separated characteristics affected by cooling rate of immiscible Cu-Cr alloy by laser surface melting, *Journal of Alloys and Compounds* (2018), doi: 10.1016/j.jallcom.2018.08.012.

Phase separated characteristics affected by cooling rate of immiscible Cu-Cr alloy by laser surface melting

Litian Zhang[a, b], Gang Yu[a, b,*], Xiuli He[a, b], Shaoxia Li[a], Weijian Ning[a], Xu Wang[a, b]
[a] Institute of Mechanics, Chinese Academy of Sciences, Beijing 100190, China
[b] School of Engineering Science, University of Chinese Academy of Sciences, Beijing 100049, China

Key Words: Cu-Cr immiscible alloy
Liquid phase separation (LPS)
Laser surface melting (LSM)
Microstructure

Abstract

The effect of cooling rates on the solidified microstructure of Cu-50Cr (wt. %) produced by laser surface melting (LSM) was studied. Layered structure transformed into a dispersed structure when the cooling rate increased from ~10^5K/s to ~10^6K/s. The average diameter of the Cr-rich spheroids in the homogenous layer was reduced to less than 1μm, and the migration velocity by Maragoni motion was ~10^3 times higher than the velocity by Stokes sedimentation, suggesting that the movements of α-Cr droplets containing supersaturated Cu phase during liquid phase separation (LPS) were dominated by Marangoni motion. Although the collisions and coagulations between Cr droplets couldn't be eliminated, the growth was suppressed by high cooling rate. The melt layer presented improved homogenous microhardness and the well-dispersed melt layer exhibited higher withstanding voltage than that of the untreated.

1. Introduction

Immiscible alloys with a stable or metastable miscible gap will decompose into two mutual insoluble liquids ($L \rightarrow L_1+L_2$) when they were undercooled into liquid miscibility gap as a result of liquid phase separation (LPS) [1]. Almost 20% of binary alloy systems own the characteristics of LPS, microstructural segregation occurred easily due to density differences of the two liquids, and thus industrial applications are limited [2]. Metastable Cu-X (X=Cr, Co, Fe, etc.) alloy was potential as self-assembled materials with special physical and mechanical properties when spherical X-rich particles uniformly distributed in the Cu metallic matrix [3-5]. Cu-Cr alloys with high Cr contents (20-60 wt. %) were predominant electrical contact materials widely used in nearly all the commercial high-power (1~100kV) vacuum interrupters [6], which was worthy of investigating the method to obtain a dispersed microstructure as well as the kinetics and mechanism of LPS during solidification.

Research on Cu-Cr liquid immiscible alloys has recently been focused on investigating the formation mechanism of LPS and suppressing the spatial migration behavior of second phase droplets under rapid solidification conditions. Therefore, many rapid solidification techniques were adopted aiming at achieving a fine, homogenous microstructure. Melt spinning [7], vacuum induction melting [8], and electromagnetic levitation and splat-quenching [9] were used to improve the microstructure and investigate the solidification process. Cooper et al. [10] have observed the microstructure of Cu–Cr–Ag alloys with a Cr content between 7.7~21.4 wt. % by gas atomization, and found the spheroidal morphology of Cr phase which was attributed to metastable liquid phase separation during rapid solidification. Gao et.al [11] reported that the size of Cr phase was reduced (~100nm) as a result of increased cooling rate. However, these methods were not able to fabricate large-sized specimen. Laser surface processing has great advantages in manufacturing Cu-Cr alloys with large contact area for engineering, due to the merits of fast processing speed, a controllable heat source (laser beam) and a high cooling rate (10^{4-7}K/s) [12]. Hirose et.al [13] reported that Cu-Cr alloyed layers could be obtained by laser surface alloying of Cr powders on to a Cu substrate by CO_2 laser with laser power density of ~10^3MW/m^2, a few microns in size (2.8μm) Cr particles distributed in the alloyed layer, and found that the Cr concentration decreased from the surface to the bottom of the layer. Zhang et al. [14] produced a Cu-25,50Cr (wt. %) cladding layer without large-scale macroscopically separation by CO_2 laser with power density of ~10^2MW/m^2, whose microstructures were composed of Cr dendrites (~50μm) and several hundred micron scaled Cr phase embedded in the Cu matrix due to insufficient LPS.

Compared with laser surface cladding or alloying, laser surface melting (LSM) is one of the most efficient and economical method of laser surface processing without element additions or changes in chemical compositions. But LSM of Cu-Cr alloy was more challenging because of the high thermal conductivity and reflectance of Cu-based alloys for laser. Previous studies showed that the grain size of Cu-Al-Ni-Mn alloy could be refined to 23±5μm with laser power density up to ~10^4MW/m^2 [15].

The previous studies showed that the cooling rate was the major factor can affect the value of undercooling and the solidification microstructure of Cu-based immiscible alloys [16, 17]. However, the effect of cooling rate on the microstructure of the immiscible hypereutectic Cu-Cr alloys containing 50wt% Cr produced by LSM has rarely been reported. In the present paper, different laser scanning speeds were adopted to investigate the effect of cooling rates on microstructure evolution of phase separated Cu-Cr alloy. The solidified microstructure of the melt layer transformed from a layered structure into a dispersed structure with the increase of cooling rate, a homogeneous immiscible melt layer with refined Cr-rich spheroids (~1μm) were successfully prepared by a high power density (~10^5MW/m^2) laser beam. The improved properties of the melt layer were also studied.

2. Experimental details

Commercial Cu-50Cr (wt. %) contacts were prepared by powder metallurgy method, with a thickness of 3mm and diameter of 10mm. The surfaces of the contacts were grinded on both sides to obtain a constant roughness of 1.6±0.4μm. The LSM process was carried out in an inert atmosphere box under argon atmosphere where the content of O_2 and H_2O were kept less than 10ppm. An Nd-YAG laser with a wave length of 1064nm was selected for the treatment. The processing parameters were as follows: laser power 580W, laser scanning speed 2 and 8m/min, spot diameter 100μm. The scanning interval between adjacent tracks was kept 80μm and the surface was continuously scanned in lines which were equal to the length of the samples. In order to get a larger temperature gradient, the temperature of the substrate was kept at 288K to cool back of the sample.

After LSM, the samples were cut along the direction which was perpendicular to the laser scanning direction. Then, the samples were polished mechanically and cleaned with ethanol. The microstructure was observed by scanning electron microscope (SEM, ZEISS EVO18) with an energy dispersion spectrometer (EDS) and a backscattered electron detector. Backscattered electron images (BSD) were taken to study the microstructure of the alloy. The size of second phase particle was measured by Image-pro software. The phase constituents of surfaces of the samples were analyzed by X-ray diffractometer (XRD, with Cu Kα radiation) operating at 40kV and 120mA.

Hardness was measured on the cross-section of the melt layer by a Vickers hardness tester with a load of 250g and a dwelling time of 15s. Three pairs of untreated and three pairs of LSM treated contacts with scanning speed of 8m/min were symmetrically assembled in six vacuum interrupters to test interruption capabilities. Voltages were applied to fixed contacts and moving contacts (contact gap 2mm) respectively, until the interrupters broke down. The maximum value of the voltage was cited as the withstanding voltage. In order to reduce the destruction effects caused by standard impulse voltage, the number of tests for each vacuum interrupter was limited to 10 times.

3. Results

3.1 Microstructure

Fig.1 shows the microstructure of Cu-50Cr (wt. %) alloy before LSM treatment (BSD image), black round or elliptical Cr particles were surrounded by grey Cu phases. The key parameter for Cu-Cr alloy, the average diameter of Cr particle was approximately 81.3μm. According to the EDS analysis, the Cu matrix (marked A) containing 99.59 wt. % Cu and 0.41 wt. % Cr, the Cr particle (marked B) containing 0.20Cu wt. % and 99.80 wt. %Cr. The maximum solubility of Cu in Cr and Cr in Cu is 0.77% and 0.08% (mole fraction) at eutectic temperature, respectively [18]. Cu-Cr alloy is a binary pseudo-alloy composed of Cr particles embedded in Cu matrix.

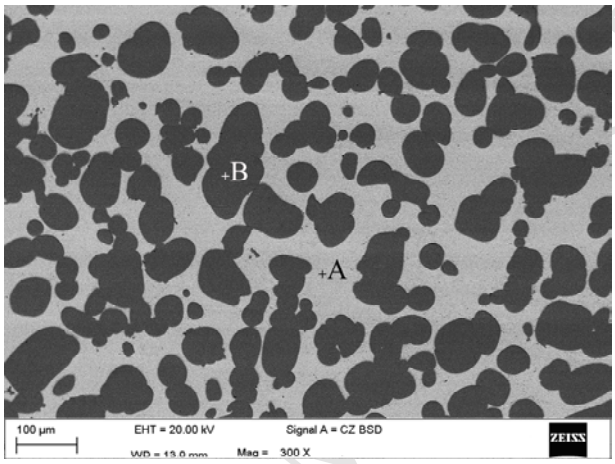

Fig.1. Microstructure of the Cu-50Cr alloy before LSM, mark capital A denoted for Cu phase and mark capital B denoted for Cr phase.

Fig. 2 (a) presents the XRD patterns of the untreated sample and samples subjected to LSM with different scanning speeds. All the diffraction peaks can be indexed to Cu and Cr phases which mainly composed of face-centered cubic (fcc) ε-Cu with peaks point to (111), (220), (200) and body-centered cubic (bcc) α-Cr with peaks point to (110), (211), (200). It could be seen from the results of XRD that there was no peak corresponding to any new phase or metallic compounds, indicating that phase transformation did not occur during LSM of Cu-Cr alloy. Fig.2 (b) illustrates the enlarged image of the Cu and Cr diffraction peaks, the intensities of the peaks Cu (111) and Cr (110) were much stronger when the laser scanning speed increased to 8m/min.

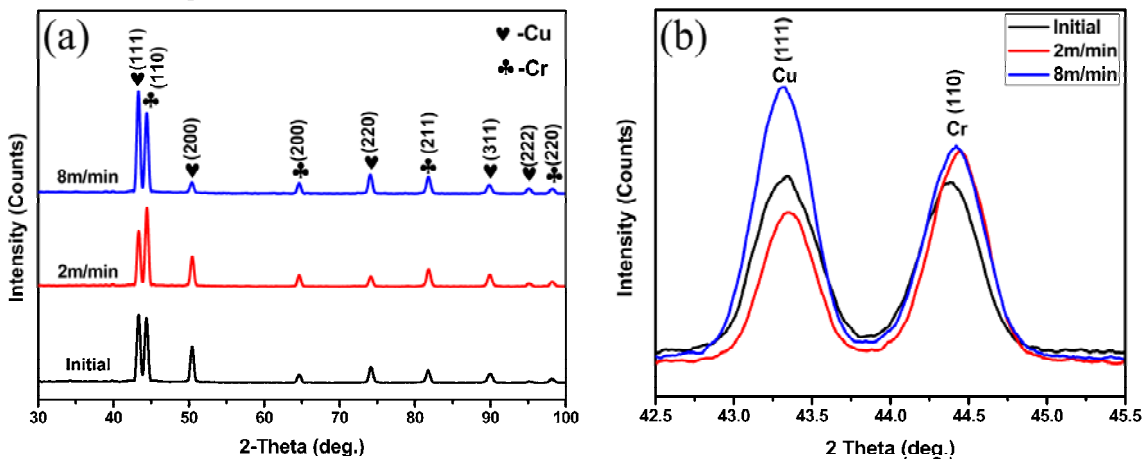

Fig.2. (a) XRD patterns of the Cu-50Cr sample before and after LSM treatment and (b) enlarged image of the Cu and Cr diffraction peaks.

Fig.3 shows the cross section of the melt layer with the laser scanning speed of 2m/min. A top-bottom separated macroscopic duplex structure was formed, the depth of the melt layer was about ~400μm with unmelt Cr phase at bottom of the melt pool, as shown in Fig. 3(a). According to the results of EDS analysis, the metallic matrix (marked C in Fig. 3(b)) of the melt layer at the top of the melt pool contained 70.89 wt. % Cr and 29.11wt. % Cu, indicating that it was a Cr-rich layer. The Cr-rich particle (marked by D in Fig. 3(b)) containing a supersaturated Cr (80.14 wt. %), small amount of Cu (19.86 wt. %). At the bottom of the melt layer, the metallic matrix (marked E in Fig. 3(c)) contained 90.71% Cu and 9.29% Cr. The bilayer structure consisted of Cr-rich layer acting as the upper layer and the Cu-rich layer as the lower layer. As shown in Fig. 3(b), the Cr-rich phase shows dual morphologies, spheroids and bands. There existed large amount of irregular shaped Cr-rich bands with a few to tens of microns in length in the upper layer, and the maximum length was 47μm. Quantities of white nano-sized Cu grains (~900nm) precipitated in the majority of Cr-rich particles. Large Cr-rich particles with sheeted shape showed a tendency to float upward to the top of the melt pool. Small Cr-rich spheroids were attached to the neighboring Cr-rich bands to minimize individual surface energy.

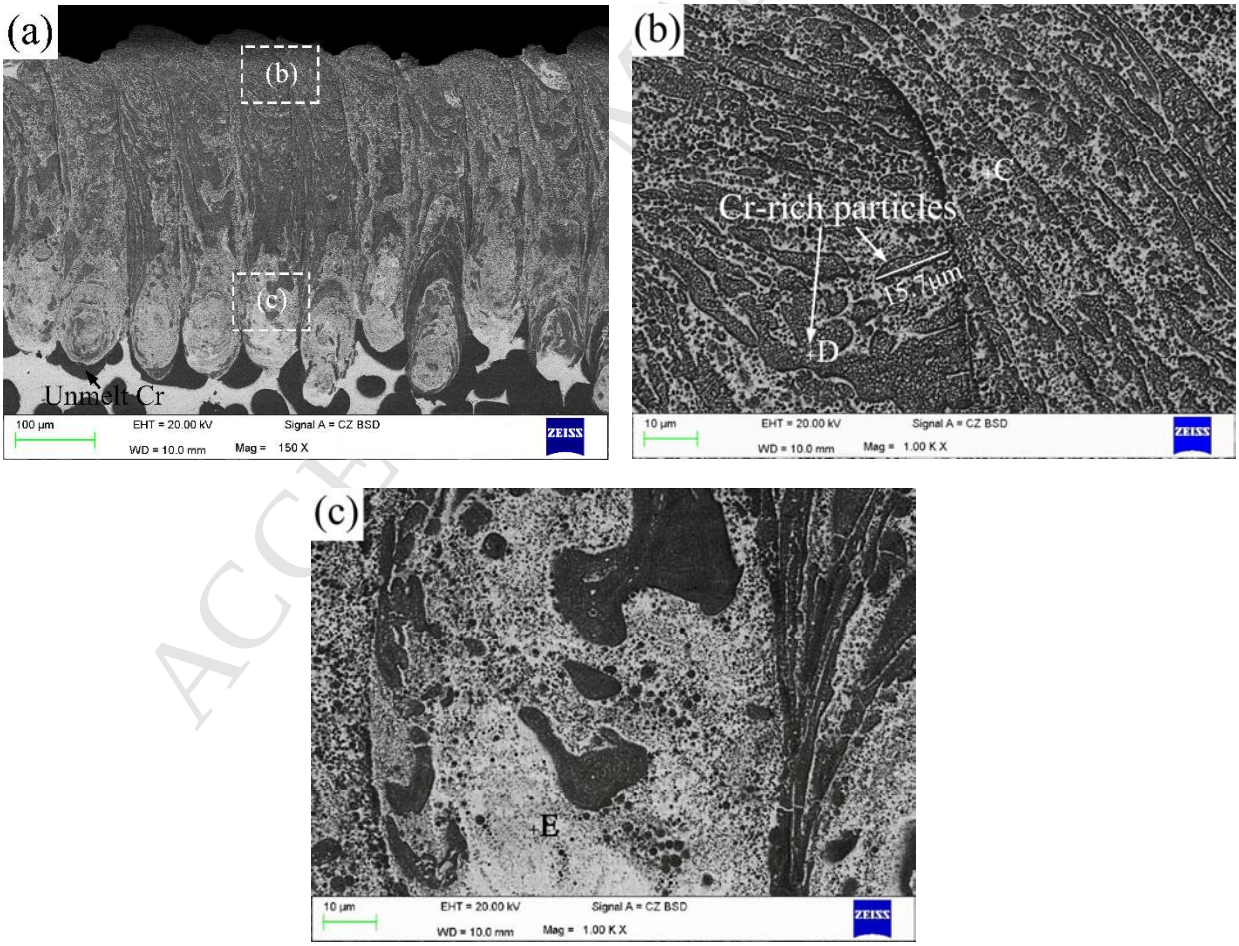

Fig.3. The cross-sectional microstructure of the melt layer of Cu-50Cr (wt. %) by LSM with laser scanning speed of 2m/min: (a) an overall view of the melt layer, (b) magnified image of zone b in

(a), mark capital C denoted for Cu-rich phase and mark capital D denoted for Cr-rich phase, (c) magnified image of zone c in (a), mark capital E denoted for Cu-rich phase.

Fig.4 shows the cross-sectional microstructure of the melt layer with the laser scanning speed of 8m/min. A homogenous refined layer was formed and the depth of the melt layer is nearly ~200μm (Fig. 4(a)), and the Cr phase at the bottom of the melt layer was partly melted, an interface between the melt and un-melt layers can be detected. Fig. 4(b) showed the microstructure at the top of the melt layer, the average size of Cr particles was ~0.9μm and the maximum radius was ~4μm. Large amount of Cr spheroids were well-dispersed in the Cu matrix, while the clustering tendency between Cr dots were not frequently observed compared with Fig.3 (b). Fig. 4(c) presents the microstructure at the bottom of the melt layer, white nano-sized Cu phase (~100nm) precipitated in some of the Cr-rich particles and the average diameter of the Cr particles was ~0.8μm and the maximum radius was ~3μm. The EDS results indicated that the Cr-rich particle (marked F in Fig. 3 (c)) containing 74.86 wt. %Cr and a supersaturated 25.14 wt. % Cu. According to the results of XRD, the melt layer is composed of α-Cr and ε-Cu phases. Compared with the untreated alloy and the laser melt sample (2m/min), a minor shift of Cu peaks to lower angle was observed for the laser melt sample (8m/min). It implied that the plane spacing was increased according to Bragg equation, which may be attributed to the formation of Cu-Cr solution prepared by rapid solidification.

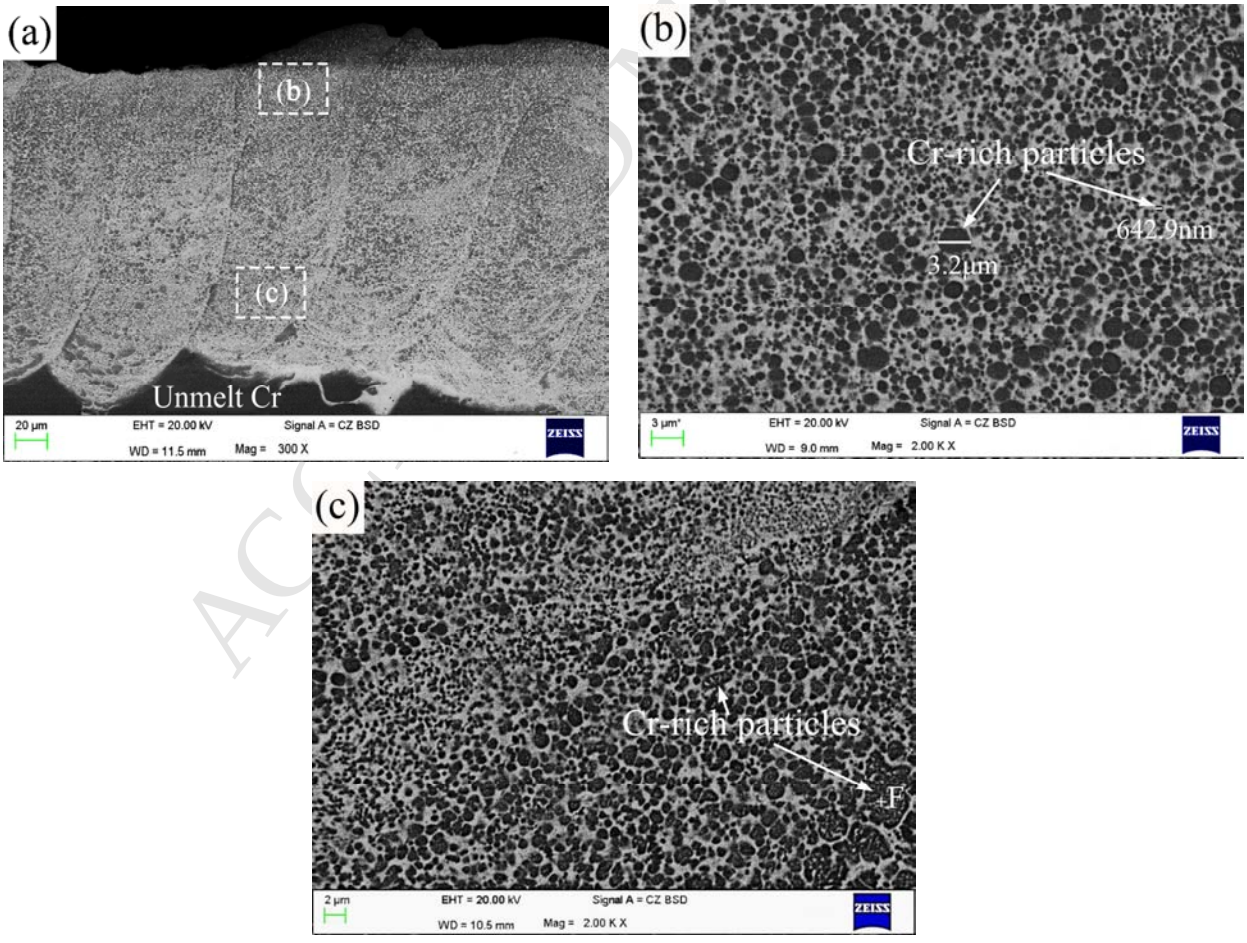

Fig.4. The cross-sectional microstructure of the melt layer of Cu-50Cr (wt. %) by LSM with laser

scanning speed of 8m/min: (a) an overall view of the melt layer, (b) magnified image of zone b in (a), (c) magnified image of zone c in (a).

3.2. Properties

3.2.1 Microhardness of the melt layer

Fig.5 shows the microhardness distribution of cross section of the melt layer with the scanning speeds of 2m/min and 8m/min. Each indentation was measured in intervals of 30μm parallel to the surface. It can be seen that when the scanning speed was 2m/min, the microhardness of the melt layer showed a sharp gradient characteristics, which was accordance with the demixing structure. The average hardness of the Cr-rich layer ($257HV_{0.25}$) was 1.4 times higher than that of the Cu-rich layer ($180HV_{0.25}$). However, the microhardness distribution was uniform when the scanning speed was 8m/min, which was also accordance with the homogeneous microstructure. The average hardness of the homogenous melt layer is ($274HV_{0.25}$), which is 3.3 times higher than that of the substrate (HB80, approximately 82HV).

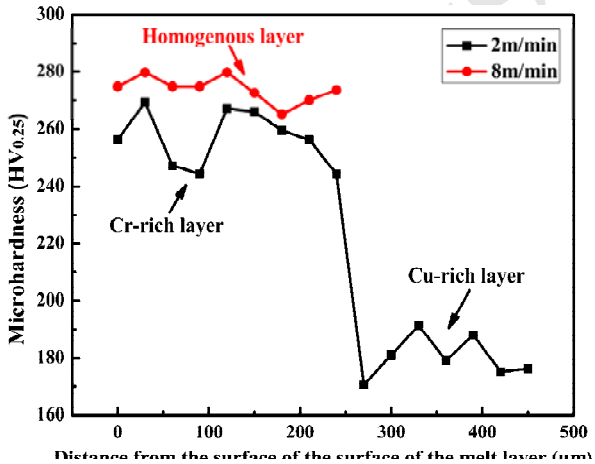

Fig.5. Microhardness distribution of cross-section of the melt layer with different laser scanning speeds.

3.2.2 Withstanding voltage and interruption capability

The appearance of the spherical shape Cr particles was beneficial for the electric properties of Cu-Cr alloy, while the large Cr sheets with irregular shapes were harmful to the performance of Cu-Cr contacts [19], so the LSM sample with homogenous microstructure (8m/min) was chosen for the interruption capability. Table.2 is the statistical analysis of the standard impulse voltage distribution of the vacuum interrupter. The $U_{average}$ represented the average value of the withstanding voltages in each vacuum interrupter, and ΔU (U_{max}-U_{min}) indicated the scattering of breakdown voltages in 10 successive experiments (the difference between the maximum breakdown voltage and the minimum breakdown voltage). When the positive standard impulse voltage was applied to the moving contact of the vacuum interrupter assembled with the laser melt samples (8m/min), the average withstanding voltage of vacuum interrupter was 123kV, which was 18.3% higher than that of the untreated (104kV). And the ΔU was 10kV, which was 28.6% lower than that of untreated (14kV).When the positive standard impulse voltage was applied to the fixed

contact of the vacuum interrupter assembled with the laser melt samples, the average withstanding voltage of vacuum interrupter is 121kV, which was 21.0% higher than the average value 100kV. And the ΔU is 9kV on average which was 66.6% lower than that of untreated (15kV). The results demonstrated that both the maximum value and stability of withstanding voltage were improved after LSM treatment.

Table.1. Withstanding voltages of untreated and LSM treated (8m/min) samples.

Withstand voltage / Surface process	$U_{average}$(kV)		$\Delta U=U_{max}-U_{min}$ (kV)	
	Moving contact	Fixed contact	Moving contact	Fixed contact
Untreated (U_0)	104	100	14	15
Laser surface melting (U_1)	123	121	10	9
$(U_1-U_0)/U_0$	18.3%	21.0%	-28.6%	-66.6%

4. Discussion

4.1 Microstructure

4.1.1 Solidification characterization

The high cooling rate obtained by LSM can lead to a dynamic undercooling (ΔT) of higher than 150K, which was much higher than the required ΔT for LPS in Cu-Cr containing 50 wt. % Cr (98K) [9,20]. Therefore, when homogenous Cu–Cr melt was cooled below the metastable miscible gap (MG), the melt decomposed into two mutual insoluble melts spontaneously, i.e., Cu-rich liquid ($L_{Cu-rich}$) and Cr-rich liquid ($L_{Cr-rich}$). The Gibbs free energy of a liquid and a solid was higher than that of the two liquids, so the solidification of primary crystals stopped when LPS occurred. At the beginning of LPS, both Cu-rich and Cr-rich liquid were in the supercooled state and tended to nucleate, critical energy required for nucleation can be given as follows [21]:

$$\Delta G_c = \frac{16\pi}{3}\frac{(\gamma T_m)^3}{(L_m \Delta T)^2} \quad (1)$$

Where ΔG_c is the critical nucleation work of forming a critical nucleus, γ is the surface energy per unit area of embryos, T_m is the liquid temperature, ΔT is the undercooling of the liquid, L_m is the latent heat of liquid-solid transformation, respectively. Based on equation (1), ΔT, as a stimulating force for nucleation, presents an inversely proportional relationship with ΔGc. According to the binary diagram in Fig.6 [18], Cr-rich liquid always experienced a higher ΔT than that of Cu-rich liquid. Therefore, it could be seen that Cr-rich liquid possessed a relatively smaller ΔG_c, suggesting that the Cr-rich phase gained the priority to nucleate. In accordance with the experimental results, the Cr-rich phase always solidified as the second phase droplets and showed the characteristics of rapid solidification.

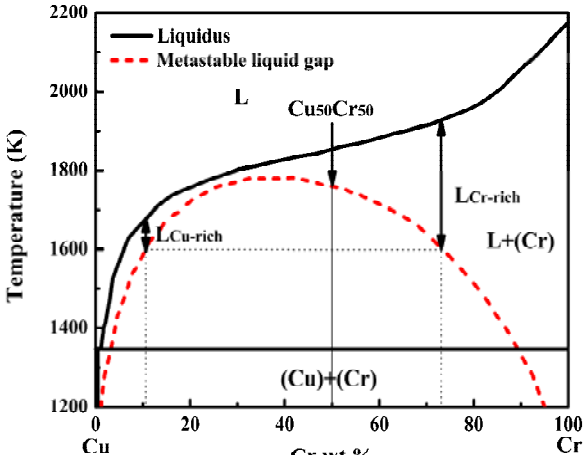

Fig. 6. Phase diagram of Cu-Cr binary alloy system with a metastable miscible gap produced from Ref. [18]. The dashed line indicates the binodal line of the metastable miscibility gap.

The cooling rate had a pronounced effect on solidification microstructure of the alloy during LSM. In order to obtain temperature profiles of the melt pool, a simple numerical solution was adopted [22, 23]:

$$T = T_0 + \frac{\alpha \cdot p}{\pi^{1.5} \cdot \lambda \cdot r} \int_0^{\infty} \left(\frac{1}{1+s^2} \exp\left(-\frac{s^2}{1+s^2} \times \left[\left(\frac{x}{r} - \frac{\rho c V r}{4\lambda s^2} \right)^2 + \left(\frac{y}{r} \right)^2 \right] \right) - s^2 \left(\frac{z}{r} \right)^2 \right) ds \quad (2)$$

where T_0 is the ambient temperature, P is the laser power,α is the absorption coefficient for laser beam, r is the radius of laser spot, k is the thermal conductivity coefficient, ρis the density and c is the thermal capacity, respectively. The temperature gradient can be calculated by:

$$G = \frac{\partial T}{\partial z} \quad (3)$$

When the laser speed is in the range of 0.1~10 mm/min, the average solidification rate is very close to the laser scanning speed, so the cooling rate R can be described by [24]:

$$R = G \cdot V \quad (4)$$

As shown in Fig.3 and Fig.4, clearly, the Cr phase was melt in the Cr matrix. The temperature in the melt pool was near or a little higher than the melting point of Cr, so the absorption of the alloy was 0.2 [12], the thermal conductivity λ was 244$Wm^{-1}K^{-1}$, the thermal capacity c was 423$Jkg^{-1}K^{-1}$, the density was 7.9×$10^3$$kg/m^3$, respectively. The temperature profile and the cooling rate of the melt pool during LSM were shown in Fig.7. The cooling rate increased with the increase of laser scanning speed, the change of cooling rate will result in a distinct solidification behavior.

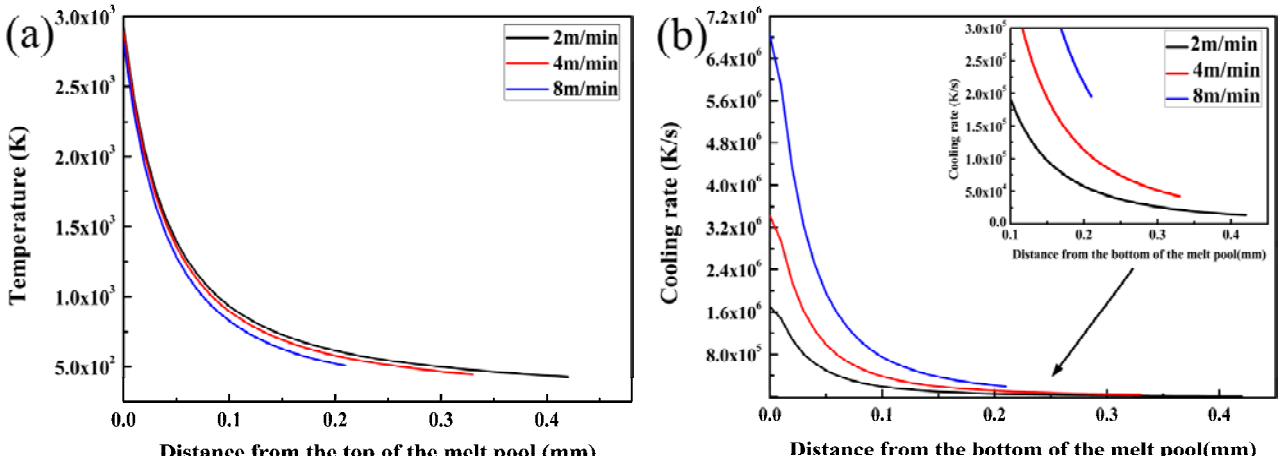

Fig.7. (a) Temperature profiles and (b) cooling rates of the melt pool during LSM with different scanning speeds.

4.1.2 The effect of second phase droplets motions on solidification

During liquid-liquid separation, the Cr-rich liquid decomposed into many spherical liquid droplets driven by surface tension to minimize overall surface energy. However, these droplets were thermodynamically unstable, they could move relatively to each other and to the liquid matrix. The spatial migrations of Cr-rich droplets were dominated by Marangoni motion and Stokes sedimentation, and the collisions and coagulations of droplets were influenced by droplets motions. In the process of LPS, Cr-rich droplets would collide and accumulate into a new, even larger droplet. The movement velocity of droplet induced by Marangoni motion due to temperature gradient was written as follows [3, 25]:

$$V_m = \frac{2}{3} \cdot \frac{\frac{\partial \sigma}{\partial T} \cdot G}{3\eta_d + 2\eta_m} \cdot r \quad (5)$$

where r is the radius of the liquid droplet, η_m is the viscosity of the matrix, η_d is the viscosity of liquid droplets, $\partial\sigma/\partial T$ is the temperature dependent coefficient of interfacial energy, respectively, G stands for the temperature gradient, respectively. The velocity of liquid droplets induced by Stokes sedimentation due to gravity was described as follows [3, 25]:

$$V_s = \frac{2}{3} \cdot \frac{\Delta\rho(\eta_d + \eta_m)g}{\eta_m(3\eta_d + 2\eta_m)} \cdot r^2 \quad (6)$$

where g is the acceleration due to gravity and $\Delta\rho$ is the density difference between two liquids. The interfacial energy between two immiscible liquids could be expressed by the equation (7) [5, 26]:

$$\sigma = \frac{6.05T_c + 7T}{1.06(\sum X_a V_a)^{2/3}(N_{AV})^{1/3}} \left(1 - \frac{T}{T_c}\right)^{1.26} \quad (7)$$

where T_c is the critical temperature above which all the alloys become homogeneous, N_{AV} is the Avogadro's number, and X_a and V_a are the mole fraction and molar volume of the component, respectively. The interfacial energy and its dependence of temperature were given in Fig.8, the interfacial energy decreased considerably with increasing temperature.

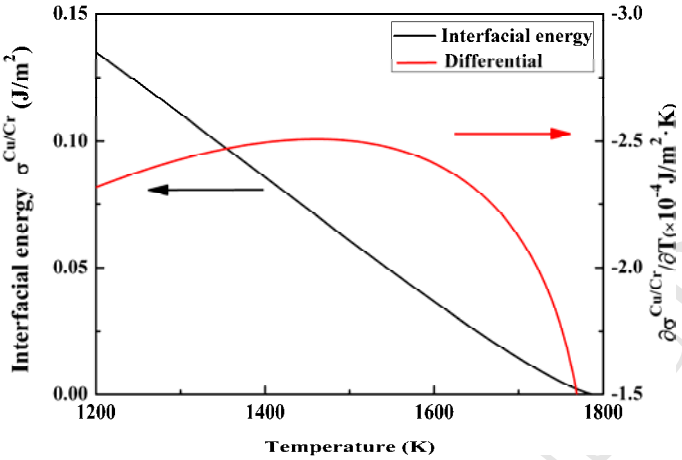

Fig.8. Interfacial energy and its differential between two liquid phases of the Cu-50Cr (wt. %) alloy.

The viscosities of the melt were calculated by equation (8) [27]:

$$\eta = 5.7\times10^{-6}\frac{\sqrt{M\cdot T_m}}{V_m^{2/3}} \quad (8)$$

where M is the atom weight, and V_m is the atom volume at temperature T_m. The parameters used in the calculation for V_m and V_s are summarized in Table 2.

Table.2. Parameters used to calculate the temperature and motions of the droplets.

Parameters	Value	Unit	Reference
Viscosity of Cu liquid, η_m	4×10^{-3}	Ns/m^2	[28]
Viscosity of Cr droplet, η_d	3.5×10^{-3}	Ns/m^2	Extrapolated from μ_m
Density of Cu liquid, ρ_1	7.9×10^{3}	kg/m^3	[29]
Density of Cr liquid, ρ_2	6.7×10^{3}	kg/m^3	[29]
Critical temperature, T_c	1787	K	[18]
Molar volume of Cu, V_{Cu}	7.82×10^{-6}	m^3/mol	[5]
Molar volume of Cr, V_{Cr}	7.54×10^{-6}	m^3/mol	Extrapolated from V_{Cu}
$\partial\sigma/\partial T$	2.4×10^{-4}	Jm^{-2}K^{-1}	This work
Gravitational acceleration	9.8	m/s^2	[3]

Migration velocities induced by Stokes sedimentation and Marangoni motion of Cr droplets in undercooled Cu-50Cr melt (8m/min) was calculated at 1549K where temperature gradient was 162716.7K/m. There was a cross-point $r_{critical}$=1771.1μm in the velocity curves where the values of V_s was equal to V_m. Increasing laser scanning speed can decrease temperature gradient G, which resulting in the decreasing of V_m/V_s. Therefore, the critical radius for the sample with scanning speed of 2m/min

was even larger than 1771.1μm. As illustrated in Fig.4, when the average radius of Cr-rich particles was about ~0.5μm, the ratio of V_m/V_s was 3.54×10^3, indicating that it was the Marangoni motion that dominated the movement of the Cr-rich droplets. Since Cu-rich matrix was denser than Cr-rich droplets, the light Cr-rich phases will flow up under the influence of Stokes sedimentation. Meanwhile, Marangoni motion accelerated the upward migration of Cr-rich droplets to the top of the melt pool where the temperature was higher. Under the combined effect of both Stokes sedimentation and Marangoni motion, the Cr-rich droplets will move upwards strongly. If time permitted, these Cr-rich droplets will also collide and coalescence continuously and they could reach to a size of tens of microns with a few seconds due to a collision-assisted accumulation in the Cu-rich matrix. As shown in Fig.3 (b), as the laser scanning speed decreased to 2m/min which provided more time for the melt pool. The Cr-rich droplets grew, coagulated and elongated to a size up to tens of microns, the Cr-rich layer with band-shaped Cr-rich particles was formed due to fierce collisions and accumulations. While the Cu-rich layer sank to the bottom of the melt pool. Macroscopic segregation was observed, a clear boundary between the two layers could be detected. The microstructure morphologies observed in the melt pool implying that the severe convections, induced by thermos-capillarity, occurred in the melting pool during LSM.

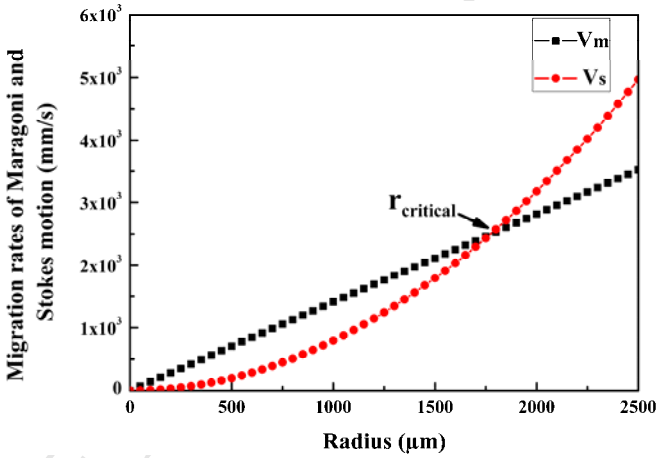

Fig.9. Calculated velocities of Marangoni motion and Stokes sedimentation versus Cr-rich droplet radius.

4.1.3 The effect of cooling rate on solidification

As shown in Fig. 7(b), increasing laser scanning speed can increase the cooling rate of the melt pool in the process of LSM. When the scanning speed is 8m/min, the cooling rate was up to 6.8×10^6K/s near the bottom of the melt pool, and up to 1.9×10^5K/s at the surface of the melt pool. The average cooling rate of the melt layer was 1.6×10^6K/s. The interval between LPS and the start of solidification was relatively short, the Cr-rich droplets with an average size less than 1μm dispersed in the Cu-rich matrix before complete solidification (Fig. 4). These droplets were frozen within the Cu-matrix for the time was not enough for Cr-rich droplets to fully aggregate, the solidified structure is characterized by fine droplet-shaped Cr-rich particles uniformly distributed in the Cu-rich matrix. Meanwhile, the average size of

Cr-rich particles in the homogenous layer did not present obvious increasing tendency form the bottom to the surface of the melt pool, as mentioned by other researchers [28]. This is due to insufficient Marangoni motion between droplets, so Cr-rich spheroids randomly dispersed in Cu matrix without notable clustering tendency. This process was shown in Fig.10 of index 1. When the scanning speed was 2m/min, the cooling rate near the surface of the melt pool decreased to 1.4×10^{4}K/s, and the average cooling rate of the melt layer was 2.1×10^{5}K/s. The cooling time was prolonged and the formation of top-bottom separated macroscopic duplex structure was attributed to the growth and accumulation between Cr-rich droplets (Fig.10 of index 2).

According to Fig. 3(b) and Fig.4(c), the substructure of the Cr-rich particles was observed, quantities of white nano-scaled Cu-rich precipitates within the Cr-rich particles, which was induced by a second LPS. The Cr-rich droplets containing supersaturated Cu would nucleate and solidify before Cu-rich matrix. The Cu concentrations in Cr-rich particles were reduced to maintain the solute balance with the matrix. As temperature decreased, the Cu-rich phase would solidify when it was cooled below the melting temperature of Cu. Due to the latent heat of crystallization released from the solidification of Cu-rich melt, part of the Cr-rich particles were fully melted. These Cr-rich droplets could enter into the MG again and trigger the secondary LPS. As shown in Fig.3 (b) and Fig.4 (c), nanostructured Cu-rich grains precipitated within the spherical Cr-rich particles. However, most of the Cr-rich particles in the Cr-rich layer precipitated nano-sized Cr-rich grains (demonstrated in Fig.3 (b)), while less particles precipitated Cu-grains in the homogenous layer (shown in Fig. 4 (c)). The more completely the LPS proceeded, the more Cu-rich phase precipitated in Cr-rich particles. Therefore, the increase the cooling rate contributed to shorten the process of LPS and result in reducing the amounts of Cu grains precipitated in Cr-rich particles.

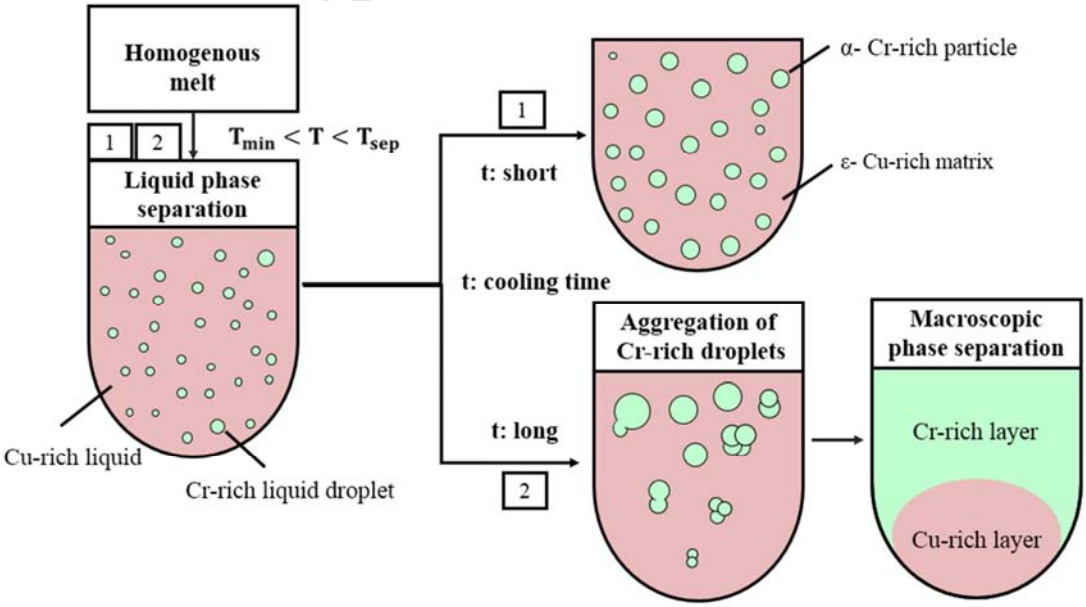

Fig.10. The schematic diagram of the formation process of the solidified microstructure for Cu-50Cr alloy.

4.2 Properties

4.2.1 Microhardness

The microhardness depended mainly on the microstructure, large amount of Cr-rich particles uniformly distributed in the Cu-rich matrix which play an important role in strengthening the Cu-Cr melt layer by LSM. According to Orowan strengthening theory, the reinforcing effect of the particles was inversely proportional to the average distance between particles [30]. The average distance between Cr-rich particles in the Cr-rich layer in duplex structure (2m/min) was larger than that of the homogenous layer (8m/min). The reinforcing effect of Cr-rich particles in the homogenous layer was stronger. In addition, the size of Cr phase in the homogenous melt layer was smaller than that of the Cr-rich layer in the duplex layer. As a result, the microhardness of the uniform layer ($274Hv_{0.25}$) was relatively higher than that of the Cr-rich layer ($257Hv_{0.25}$) in the macroscopic separated sample. For the sample with laser scanning speed of 2m/min, the Cu-rich layer contains a relatively higher Cu content compared to Cr-rich layer, resulting in a decrease of microhardness ($180Hv_{0.25}$) .

4.2.2 Breakdown strength

Vacuum electrical breakdown presents selectivity for Cu-Cr alloy, which is always concentrated on the phase with lower working functions. Breakdown was caused by the increasing amounts of electron emission when the voltage was increased. The electron emission current remarkably increased with the decrease of the working function at a given electric field intensity [31]. The first principle calculations were performed utilizing the density functional theory to calculate the work functions of pure bcc-Cr and fcc-Cu with different single crystal planes, the values were listed in Table.3 [32]. It can be seen from Table.4 that these work functions of different surfaces were in a rising order: Cr (111)＜Cr (100)=Cu (110) ＜Cu (100) ＜Cr (110) ＜Cu(111). The largest work function presents on the close-packed plane for pure Cu and Cr. Even though there were several crystal planes in CuCr50 alloy, the surfaces of Cu (111) and Cr (110) were the most stable surfaces. With the preferred growth of Cu (111) and Cr (110) orientations (Fig.2b), the work function increased compared with that of the untreated. Meanwhile, the refinement and hominization of Cr phase also contributed to mitigate serious partial ablate of the surfaces and uniformly distribute vacuum arc energy on the whole surface. Consequently, the surface of LSM treated contacts was able to withstand higher voltage (125kV), and the possibility of failures in switching off operations were reduced.

Table.3. Calculated work functions of Cu and Cr.

Element	Cu			Cr		
Surface	(111)	(110)	(100)	(111)	(110)	(100)
ϕ(eV)	4.58	4.27	4.30	3.78	4.44	4.27

5. Conclusion

The cooling rate was a key parameter to influence the solidification of hypermonotectic Cu-50 wt. %Cr alloy. The effect of second phase motions was also investigated.

(1) The final solidified microstructure of the Cu-50Cr (wt. %) melt layer was strongly affected by cooling rate. Moving Cr-rich droplets were frozen in the Cu-rich matrix due to lack of time to grow when the average cooling rate increase to ~10^6K/s, so a homogenous melt layer with α Cr-rich spheroids with average diameter less than ~1μm dispersed in ε Cu-rich matrix was obtained.

(2) The microhardness distribution was uniform when the Cr-rich spheroids were dispersed in the melt layer, the hardness ($274Hv_{0.25}$) was 3.3 times higher than that of the substrate, and was higher than that of the Cr-rich layer ($257Hv_{0.25}$) in the macroscopic microstructure due to grain refinement strengthening and dispersion strengthening.

(3) The dispersed microstructure and the increase of the peaks of Cu (111) and Cr (110) (high working function orientations) of the melt layer contributed to the improvement of withstanding voltage of fixed contacts (20.1%) and moving contacts (18.3%).

Acknowledgements

The authors would like to acknowledge financial support from the instrument developing project of the Chinese Academy of Sciences (No.yz201636) and the national natural science foundation of China (No.11672304, No. 11502269, No.11272316 and No.11272317).

Reference

[1]. J. He, J.Z. Zhao, L. Ratke, Solidification microstructure and dynamics of metastable phase transformation in undercooled liquid Cu–Fe alloys, Acta Mater. 54 (2006) 1749-1757.

[2]. R.P. Shi, C.P Wang, D. Wheeler, X.J. Liu, Y. Wang, Formation mechanisms of self-organized core/shell and core/shell/corona microstructures in liquid droplets of immiscible alloys, Acta Mater. 61 (2013) 1229-1243.

[3]. C.P. Wang, X.J. Liu, I. Ohnuma, R. Kainuma, K. Ishida, Formation of immiscible alloy powders with egg-type microstructure. Science 297 (2002) 990-993.

[4]. Gouthama, G.B. Rudrakshi, S.N.Ojha, Spray forming and wear characteristics of liquid immiscible alloys, J. Mater. Process Tech. 189 (2007) 224-230.

[5]. B. Ma, J. Li, Z. Peng, G. Zhang, Structural morphologies of Cu-Sn-Bi immiscible alloys with varied compositions, J. Alloy. Comp. 535 (2012) 95-101.

[6]. P.G. Slade, The Vacuum Interrupter: Theory, Design and Application, CRC Press, New York, 2008.

[7]. Z.B. Sun, Y.H Wang, J. Guo, Y.M Zhu, X.P. Song, R.H. Zhu, Liquid and solid phase separation during melt spinning and annealing in melt-spun Cu–Cr ribbons, Mater. Sci. Eng. A 452(2007) 411-416.

[8]. C.Y. Zhang, Y.P. Wang, Z.M. Yang, Y. Guo, B.J. Ding, Microstructure and properties of vacuum induction melted CuCr25 alloys, J. Alloy. Comp. 366 (2004) 289-292.

[9]. J. Gao, Y.P. Wang, Z.M. Zhou, M. Kolbe, Phase separation in undercooled Cu–Cr melts, Mater. Sci. Eng. A. 2007, 449 (2007) 654-657.

[10].K.P. Cooper, J.D. Ayers, J.C. Malzahn Kampe,C.R. Feng, I.E. Locci, Microstructural evolution and thermal stability in rapidly solidified high-chromium-containing copper alloys, Mater. Sci. Eng. A 142 (1991)221-233.

[11].Z.M. Zhou, Y.P. Wang, J. Gao, M. Kolbe, Microstructure of rapidly solidified Cu−25wt.% Cr alloys, Mater. Sci. Eng. A 398 (2005) 318–322.

[12].J.D. Majumdar, R. Galun, B.L. Mordike, I. Manna, Effect of laser surface melting on corrosion and wear resistance of a commercial magnesium alloy, Mater. Sci. Eng. A 361 (2003) 119-129.

[13].A. Hirose, K.F. Kobayashi, Surface alloying of copper with chromium by CO_2 laser, Mater. Sci. Eng. A 174 (1994) 199-206.

[14].S.H. Si, H. Zhang, Y.Z. He , M.X. Li, S. Guo, Liquid phase separation and the aging effect on mechanical and electrical properties of laser rapidly solidified $Cu_{100-x}Cr_x$ alloys, Metals 5 (2015) 2119-2127.

[15].M.R. Silva, P. Gargarella, T. Gustmann, W.J.B. Filho, C.S. Kiminami, J. Eckert, S. Pauly, C. Bolfarini, Laser surface remelting of a Cu-Al-Ni-Mn shape memory alloy, Mater. Sci. Eng. A. 661 (2016) 61–67

[16].Y. Qi, L. Wang, S.H. Wang, X.L. Li, W.C. Cui, Structural and dynamical heterogeneity of undercooled $Fe_{75}Cu_{25}$, melts with miscibility gap, J. Alloy. Comp. 615 (2014) 962-968.

[17].A. Munitz, A. Venkert, P. Landau, M.J. Kaufman, R. Abbaschian, Microstructure and phase selection in supercooled copper alloys exhibiting metastable liquid miscibility gaps, J. Mater. Sci. 47 (2012) 7955-7970.

[18].K.T. Jacob, S. Priya, Y.A. Waseda, Z. Metallkd, Thermodynamic Study of Liquid Cu-Cr Alloys and Metastable Liquid Immiscibility, Z. Metallkd. 91 (2000) 594–600.

[19].X. Wei, J.P. Wang, Z.M. Yang, Z.B. Sun, D.M. Yu, X.P. Song, B.J.Ding, S. Yang, Liquid phase separation of Cu–Cr alloys during the vacuum breakdown, J. Alloy. Comp. 509 (2011) 7116-7120.

[20].S.F Zhou, X.Q. Dai, C.X. Wang, M. Xie, J.X. Yang, Z.Y. Li, Phase separated characteristics and soft magnetic properties of $[Cu_{0.6}(FeCrC)_{0.4}]_{100-x}Si_x$ immiscible composites by laser induction hybrid cladding, J. Alloy. Comp. 732 (2018) 740e747

[21].T.B. Massalski, C.G. Woychik, Modelling of the nucleation temperature of the f.c.c. Phase competing with glass formation in Cu-Ti alloys, Acta Metall. 33 (1985)1873-1886.

[22].H.E. Cline, T.R Anthony, Heat treating and melting material with a scanning

laser or electron beam, J. Appl. Phys. 48 (1977) 3895-3900.

[23].M. Picasso, C.F. Marsden, J.D. Wagniere, A. Frenk, M. Rappaz, A simple but realistic model for laser cladding, Metall. Mater. Trans B. 25 (1994) 281-291.

[24].A. Frenk, W. Kurz, High speed laser cladding: solidification conditions and microstructure of a cobalt-based alloy, Mater. Sci. Eng. A 173 (1993) 339-342.

[25].R.P Shi, Y. Wang, C.P. Wang, X.J. Liu, Self-organization of core-shell and core-shell-corona structures in small liquid droplets, Appl. Phys. Lett. 98 (2011) 15-17.

[26].G. Kaptay, A Calphad-compatible method to calculate liquid/liquid interfacial energies in immiscible metallic systems, Calphad, 32 (2008) 338-352.

[27].E.N. Andrade, A theory of the viscosity of liquids, Philos. Mag. 17 (1934) 497-698.

[28].X. Dai, M. Xie , S. Zhou , C. Wang , M. Gu, J.X. Yang, Z.Y. Li, Formation mechanism and improved properties of Cu95Fe5 homogeneous immiscible composite coating by the combination of mechanical alloying and laser cladding, J. Alloy. Comp. 740 (2018) 194-202.

[29].T. Iida, R.I.L. Guthrie, The Physical Properties of Liquid Metals, Clarendon Press, Oxford, 1988.

[30].A. Kelly, R.B. Nicholson, Strengthening methods in crystals, Elsevier, Amsterdam, London, New York, 1971.

[31].Y. Hirata, K. Ozaki, U. Ikeda, M. Mizoshiri, Field emission current and vacuum breakdown by a pointed cathode, Thin Solid Films. 515 (2007) 4247-4250.

[32].W.C. Cao, S.H. Liang, X. Zhang, X.H. Wang, X.H. Yang, Effect of Mo addition on microstructure and vacuum arc characteristics of CuCr50 alloy, Vacuum. 85 (2011) 943-948.

Highlights

Homogenous immiscible melt layer is fabricated by laser surface melting.
Numerous α-Cr particles with diameter of ~1μm are dispersed in the ε-Cu matrix.
The sedimentation of the second phase is inhibited by high cooling rate (~10^6K/s).
Breakdown strength and microhardness is improved than that of the substrate.